Reactions $\pi^{\pm}p \to pX^{\pm}$ (1100–1500 MeV) near threshold*

W. C. Harrison,† J. Alspector,‡ K. J. Cohen, and J. Oostens§
Rutgers University, New Brunswick, New Jersey 08903‖

G. R. Kalbfleisch and V. VanderBurg¶
Brookhaven National Laboratory, Upton, New York 11973

C. M. Ankenbrandt**
Indiana University, Bloomington, Indiana 47401 ††
(Received 1 October 1975)

We observe no $A_2^{\pm}$ production in $\pi^{\pm}p$ collisions near threshold. Because our upper limits for the A_2 cross-section limit s-wave production, the rapid rise of the cross section from threshold observed by other experiments must be due to p-wave production. Discussion of this result and a comparison to the data of Binnie *et al.* are given.

INTRODUCTION

The question of whether there exists narrow structure, or splitting, in the A_2 mass region has generated considerable controversy since it was first reported.[1] Since that time there have been many attempts to confirm the existence of this effect and some of these appear to contradict the original result.[2] Considerable theoretical effort has been made attempting to explain these contradictions in terms of sensitive effects such as interference.[3] This experiment was performed with the hope of resolving these apparent conflicts by making a high-statistics high-resolution measurement. We also searched for the $\delta(965)$ which has been observed by some groups but not by others.[4] The method used was the threshold-crossing technique of Binnie *et al.*[5]

We have previously discussed our data in the $\delta(965)$ region[6] and have given a preliminary account of our data in the $A_2(1310)$ region.[7]

This paper is divided into five main sections. In Sec. I the kinematics of a missing-mass experiment at threshold are described and much of the notation used in the remainder of the paper is defined. In Sec. II the experimental apparatus is described and the mass resolution discussed. Section III discusses in some detail the analysis of the systematics of the experiment including calibration, corrections applied to the raw data, and consistency checks. Section IV deals with the analysis of the measured mass spectra, describing the fits to the data, their results, and our interpretation. In Sec. V we summarize our conclusions.

I. MISSING-MASS KINEMATICS AT THRESHOLD

Consider the reaction

$$1+2\to 3+4\,, \tag{1}$$

where 1 is the incident beam (in this experiment a positive or negative pion), 2 is the target proton, and 3 is the recoil proton. By detecting the recoil proton the invariant mass of 4 is determined by

$$m_4^2 = m_1^2 + m_2^2 + m_3^2 + 2[E_1 m_2 - (E_1 + m_2)E_3 + p_1 p_2 \cos\theta_{13}]\,. \tag{2}$$

E_i, p_i, and m_i are the laboratory energy, magnitude of the momentum, and mass, respectively, of particle i ($i=1,2,3,4$) and θ_{13} is the laboratory angle between the incident pion and the recoil proton.

The threshold condition is that particles 3 and 4 are at rest in the center-of-mass system. This implies that the velocity in the laboratory system of the recoil proton is equal to the velocity of the center of mass. Thus the laboratory momentum p_{30} of the recoil proton at threshold is given by

$$p_{30} = p_1 E_{30}/\sqrt{\Delta} = p_1 m/\sqrt{s}\,, \tag{3}$$

where Δ is the square of the total lab energy, s is the square of the total energy in the center-of-mass system, and E_{30} and m are the lab energy and mass of the recoil proton at threshold, respectively.

The mass resolution is determined by the three derivatives:

$$\partial m_4^2/\partial p_1 = 2p_3\cos\theta_{13} - 2(E_3 - m_2)p_1/E_1\,, \tag{4}$$

$$\partial m_4^2/\partial p_3 = 2p_1\cos\theta_{13} - 2(E_1 + m_2)p_3/E_3\,, \tag{5}$$

$$\partial m_4^2/\partial\theta_{13} = -2p_1 p_3\sin\theta_{13}\,. \tag{6}$$

The threshold condition yields the optimum mass resolution, since $p_3 = p_{30}$ and $\theta_{13} = 0$ give

$$\partial m_4^2/\partial p_3|_{\text{thres}} = \partial m_4^2/\partial\theta_{13}|_{\text{thres}} = 0\,. \tag{7}$$

Thus a spectrometer measuring particles pro-

duced at threshold has the advantages of a spectrometer operating at the Jacobian peak[8] (where $\partial m_4^2/\partial p_3 = 0$) and a spectrometer operating at 0° (Ref. 9) (where $\partial m_4^2/\partial \theta_{13} = 0$).

The momentum of the recoil proton is defined in terms of its fractional shift S from threshold by

$$p_3 = (1+S)p_{30}. \tag{8}$$

In the mass range considered in this paper a constant shift S implies an approximately constant proton momentum in the center-of-mass system.

Figure 1 is a kinematics plot for reaction (1) near threshold ($\theta_{13} = 2.5°$). Contours of constant missing mass are plotted as a function of p_1 and p_3. Lines of p_3 at constant shift are almost straight and nearly parallel to the p_1 axis. As can be seen, such a line of constant S defines a nearly linear mass scale with respect to p_1. Thus, up to slowly varying kinematical factors, a measurement of the cross section at constant shift as a function of beam momentum is proportional to $d\sigma/dm$.

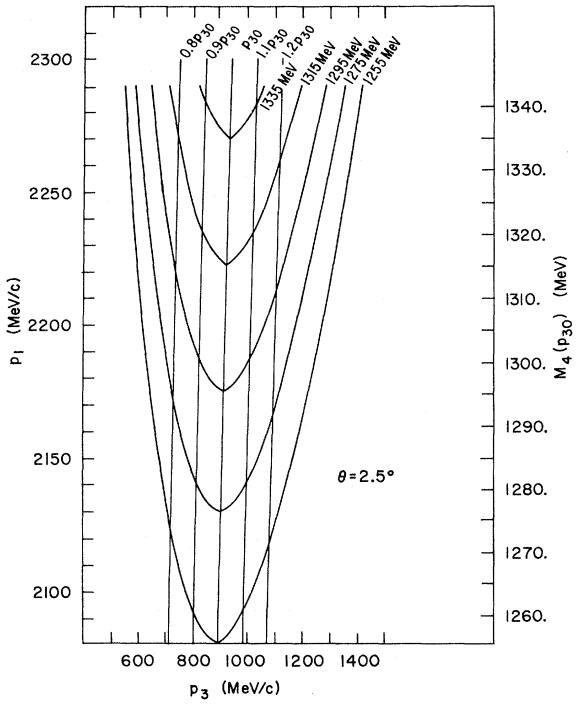

FIG. 1. Kinematics plot showing lines at constant missing mass as a function of recoil-proton laboratory momentum p_3 and incident-pion laboratory momentum p_1 at a fixed proton scattering angle θ_{13} of 2.5°. The nearly vertical lines are for proton recoil momenta equal to a constant fraction of the threshold moment p_{30}. The axis on the right gives the missing mass at threshold moment p_{30}. The axis on the right gives the missing mass at threshold.

II. DESCRIPTION OF THE APPARATUS

To investigate reaction (1) this experiment measured the momentum of the incoming pion, identified the recoil proton, and measured its momentum and angle. The apparatus has been described in a previous publication[6] and will only be summarized here.

The experiment was performed at the alternating gradient synchotron (AGS) of Brookhaven National Laboratory. Typically a flux of 1.5 million pions per pulse was taken from the G-10 internal target station of the AGS. The spill duration was typically 800–1000 msec. The pions produced at 10° were transported to the experimental area using the electrostatically separated beam 5 A. A diagram of the experimental setup is shown in Fig. 2. The pion beam was identified by time of flight over a flight path approximately 108 ft long. A 5% momentum bite was divided into seven bins separated by 0.8% by momentum hodoscopes. Interactions took place in a constant density (±0.1%) hydrogen target which was nearly surrounded by 32 scintillation counters designed to count the number of charged particles in the final state. Particles coming out at angles of 2.5°±2.5° to the beam direction passed through a focusing spectrometer consisting of three quadrupoles. Those particles within a 30% wide momentum band were focused onto counters T_6, T_7, and T_8 and their velocities measured by time of flight over a 10-m flight path. The combined momentum and velocity measurements identified the masses of these particles.

The apparatus counted the number of incident pions at a given momentum and the number of interactions producing a recoil proton within the

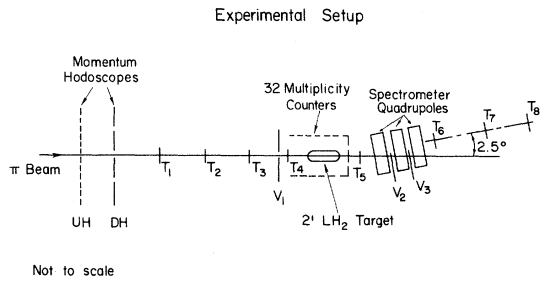

FIG. 2. Schematic of the experimental setup. The momentum hodoscopes are labeled UH and DH. The beam defining counters are T_1, T_2, T_3, and T_4. The distance from T_1 to T_4 is approximately 108 feet. V_1, V_2, and V_3 are veto counters. Thirty-two multiplicity counters nearly surround the target to count the total number of charged particles emerging from the target. The protons from the target are focused by the triplet quadrupole spectrometer onto counter T_7. The distance from T_4 to T_7 is approximately 42 feet.

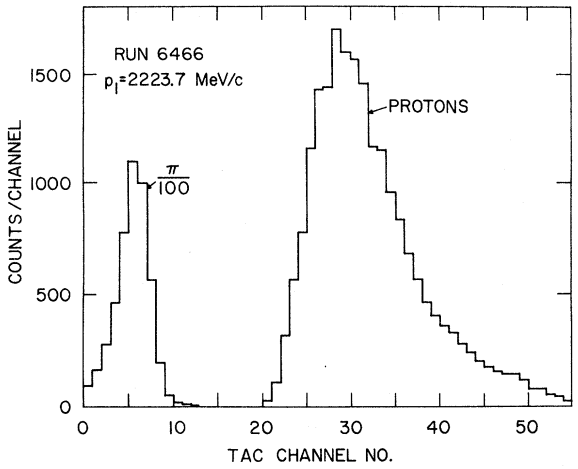

FIG. 3. A typical distribution in time of flight from T_4 to T_7. The pion peak has been divided by 100 for display.

acceptance of the forward spectrometer. The momentum—as measured by time of flight—of the recoil particle and the charge multiplicity of the final state were recorded for each interaction. Varying the beam momentum allowed us to measure the number of recoil protons per incident pion within a specified recoil momentum band as a function of the missing mass.

Figure 3 shows a sample time-of-flight distribution. The pions, which are all near $\beta=1$, are obviously cleanly separable from the protons. The center of the pion peak defines the origin of the time-of-flight axis. The shape of the proton distribution reflects not only the cross section but also the momentum acceptance of the spectrometer, which varies slightly over the mass range of this experiment. The spectrometer magnet currents were scaled in proportion to the threshold value of the recoil proton momentum as we changed beam momentum in order to accept a constant momentum bite at a constant fractional shift above threshold. However, geometrical attributes such as magnet apertures and the sizes and locations of counters remained fixed and introduce some variation in acceptance. This will be discussed further in the section on systematics.

The main data discussed in this paper were collected in three disjoint running periods. Between each period minor changes in counter sizes and spectrometer tune were made to improve counting rates. These changes require treating each data set separately. Each period includes data with both positive and negative beam, thus giving six separate data sets to discuss. Those with negative beam (i.e., negatively charged missing mass) will be labeled 1^-, 2^-, and 3^- in chronological order,

TABLE I. This table presents the FWHM values of various contributions to the mass resolution at several values of missing mass covering the range of this experiment. Γ_1 is due to the finite acceptance for recoil momentum and solid angle, Δp_3 and $\Delta\Omega_3$. Γ_2 is due to the resolution of the time-of-flight electronics. Γ_3 is due to energy losses of the incident beam and recoil protons in the liquid hydrogen target. Γ_4 is due to resolution in measuring the incident beam momentum. Γ_{tot} is the total mass resolution found by adding the individual contribution in quadrature. The values in this table were calculated for a full-width momentum bite of $\Delta p_3/p_3=0.22$, $\theta_3=2.5°\pm2.5°$ and a shift (see text) of $S=0$. However, the mass resolution was found not to change appreciably for the small changes in $\Delta p_3/p_3$ or S used in the various cuts to the data considered in Figs. 12, 14, 16, and 18.

Mass (MeV)	Γ_1 (MeV)	Γ_2 (MeV)	Γ_3 (MeV)	Γ_4 (MeV)	Γ_{tot} (MeV)
965	7	2	7	6	12
1320	6	2	6	7	11
1700	8	2	6	9	14

and those with positive beam will be labeled 1^+, 2^+, and 3^+. We consider data set 3 to be our best data set, but our conclusions are consistent with all three sets.

Within each data set we collected data in runs which lasted about one hour and which corresponded to different values of incident momentum. The incident-momentum settings were changed in increments of 2.4% until the entire range of the experiment was spanned. This procedure was then repeated twice, each time with the momentum settings offset by 0.8% (one momentum bin) relative to the previous scan. In this way the cross section at every mass was measured at least once by each of the seven incident-momentum bins as explained below. This multiplicity of measurements of each cross-section point allowed us to check our understanding of the systematic errors.

The mass spectra will typically be shown for proton-recoil-momentum bands of full width $\Delta p/p$ of 15%, centered about recoil momenta with constant shifts of −15%, 0%, and +15% from threshold. Table I gives Monte Carlo mass resolution for different masses for these bites. The contributions to the mass resolution are as follows:

Γ_1, those due to the finite Δp_3 and $\Delta\Omega_3$ bites;
Γ_2, those due to the resolution of the time-of-flight electronics;
Γ_3, those due to energy losses by beam and recoil protons in target; and
Γ_4, those due to beam momentum resolution.

As seen in Table I the total mass resolution varies slowly over the range of this experiment.

III. ANALYSIS OF EXPERIMENTAL SYSTEMATICS

A. Beam momentum

1. Absolute calibration

The beam was tuned for a nominal momentum of 1364.1 MeV/c using magnet calibrations from a previous experiment. This setting was then checked directly by measuring the time of flight of π^+, p, d^+, and T^+ over a surveyed flight path of 108 ft. The differences in times of flight for known particles of different masses uniquely determine their velocities and thus their common momentum. From the surveyed distances and known counter thicknesses we calculated the expected time of flight of each type of particle as a function of momentum. The calculations included the effect of energy losses in all intervening counters, vacuum-pipe windows, etc. The calculated differences in time of flight for several pairs of particles are plotted in Fig. 4 as a function of momentum. The measured time-of-flight differences for the same pairs of particles are also plotted where they intersect the calculated curves. Each pair gives a separate estimate of the momentum. The difference in time of flight of pions and protons as well as the difference between deuterons and tritons is less than the range of the time-to-amplitude converter (TAC) scale. The time-of-flight difference between pions and tritons was the largest we could observe and was the most sensitive measure of the momentum. To keep this time of flight on scale we had to add a measured delay. This was done in two different ways. In method I delay cable was added to the pion signal to put it on scale with the tritons. Method II consisted of adjusting a calibrated variable delay box added to the last time-of-flight counter until the pion and triton peaks fell at the same position. This method is independent of the TAC calibration. The two methods used different delays which were independently calibrated. As seen from Fig. 4 the two methods gave nearly identical results and were also consistent with the less precise results from pion-proton and deuteron-triton differences which depended only on the TAC calibration.

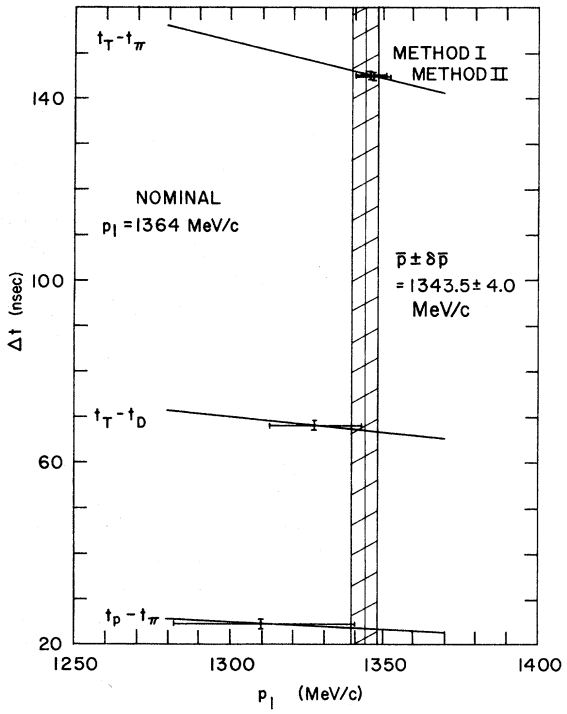

FIG. 4. The solid curves show the calculated difference in time of flight over a 1289.3-in. flight path for the indicated combination of particles as a function of the momentum of the particle at the hodoscope. The measured differences are plotted where they intersect the calculated curves and their weighted average is shown cross hatched. "Method I" and "method II" are explained in text.

The weighted average of these measurements gives a momentum of 1343.5 ± 4.0 MeV/c. This 1.5% correction means that the nominal momentum values had to be scaled by a factor of 0.985 ± 0.003.

2. Momentum hodoscope calibration

The momentum of each incident π was measured with two hodoscopes positioned near a horizontal momentum focus. A pair of counters (one in each hodoscope) determined where a particle crossed the momentum focus and therefore its momentum. This measurement was calibrated by measuring the time-of-flight distribution of particles in each pair of counters. Pairs with similar time-of-flight values were grouped into one of seven momentum bins. Tritons were used for this since they have the longest time of flight for a given momentum and thus give the most precise measurement. Figure 5 is a plot of the ratio of the momentum measured by each momentum bin to the momentum in the central (fourth) momentum bin. The straight line corresponds to a separation of 0.8% between adjacent bins. Two sets of data points are plotted: One set was taken at the beginning of the experiment and the other set at the end. The two sets are consistent, showing no long-term changes during the experiment. The error bar on the central point is inferred from the time-of-flight distribution and indicates a full width at half maximum (FWHM) of about 1% for $\Delta p_1/p_1$ for each momentum bin.

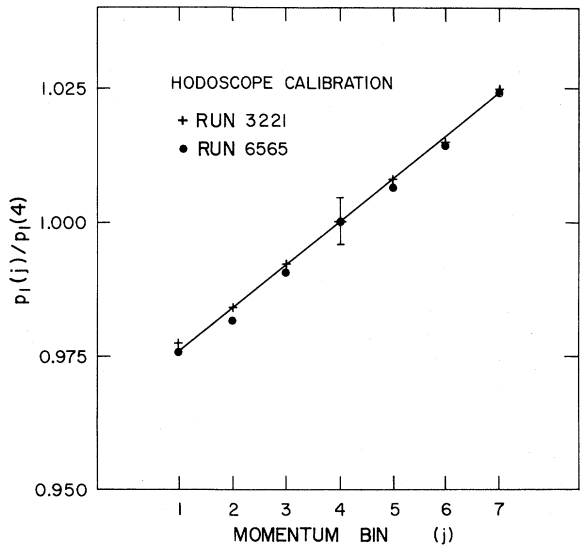

FIG. 5. The ratio of the momentum of each hodoscope bin to the momentum measured by the central bin is plotted vs bin number. Data from two different runs, one near the beginning of the experiment and the other near the end, are shown. The error bar on the central point indicates the full width at half maximum of the momentum included in one momentum bin ($\Delta p/p \approx 1\%$).

3. *Stability*

We also looked for changes in the beam momentum or our momentum measurement over time scales of the order of one run (~1 h). The first, for example, might be caused by changes in the position of the production target. For each run we computed the mean of the incident momentum distribution $\langle p_1 \rangle$ by weighting the momentum of each bin by the number of events in that bin and looked

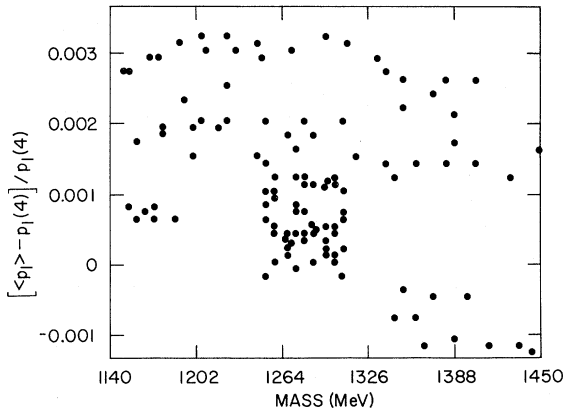

FIG. 6. The normalized deviation of the average beam momentum $\langle p_1 \rangle$ from the momentum in the central bin $p_1(4)$ is plotted vs the nominal missing mass for each run in data set 3^-.

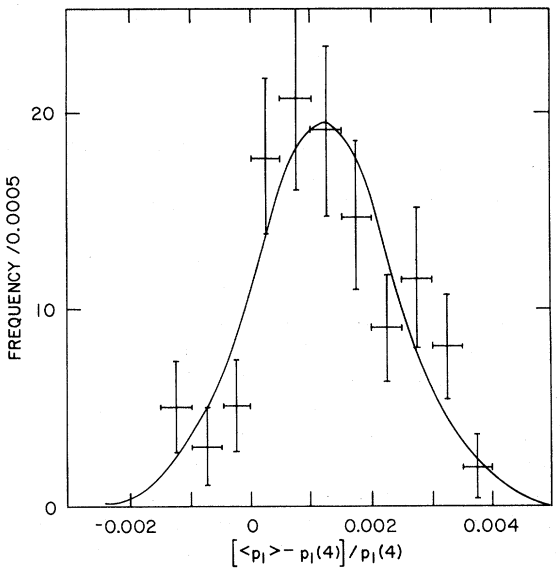

FIG. 7. Histogram of the normalized deviation $[\langle p_1 \rangle - p_1(4)]/p_1(4)$ of the average beam momentum from the momentum in the central bin is plotted for each run. The smooth curve is a fitted Gaussian.

for variations of this quantity from the nominal momentum of the central bin $p_1(4)$. Figure 6 shows the normalized residual $\langle p_1 \rangle/p_1(4) - 1$ plotted vs mass for data set 3^- and Fig. 7 shows a histogram of these residuals. There are clearly some systematic shifts. The distribution appears approximately Gaussian with a standard deviation of 0.001, indicating that the beam momentum has systematic uncertainties of ±0.1% which must be added to the ±0.3% statistical uncertainties. The displacement of the peak of the Gaussian from zero only reflects our incident momentum structure and is not important.

B. Acceptance corrections

The mass spectra (which are the result of this experiment) are plots of the number of recoil protons within a fixed angular range in the laboratory and within a momentum band of fixed fractional width $\pm f = \pm \Delta p_3/p_{30}$ centered about a momentum p_3 which is defined by the shift S from threshold [see Eq. (8)], that is, the recoil momenta accepted are within specified fractions of p_{30}, the momentum of a proton at rest in the center-of-mass system. However, as explained in the section on kinematics the threshold momentum $p_{30} = p_{30}(p_1)$ depends on the beam momentum. A change of 0.8% in p_1 from one momentum bin to the next gives a change of 0.2% in p_{30}. Thus the momentum limits of the band of protons chosen is

$$p_3 \pm \Delta p_3 = (1+S)p_{30}(p_1) \pm f p_{30}(p_1). \qquad (9)$$

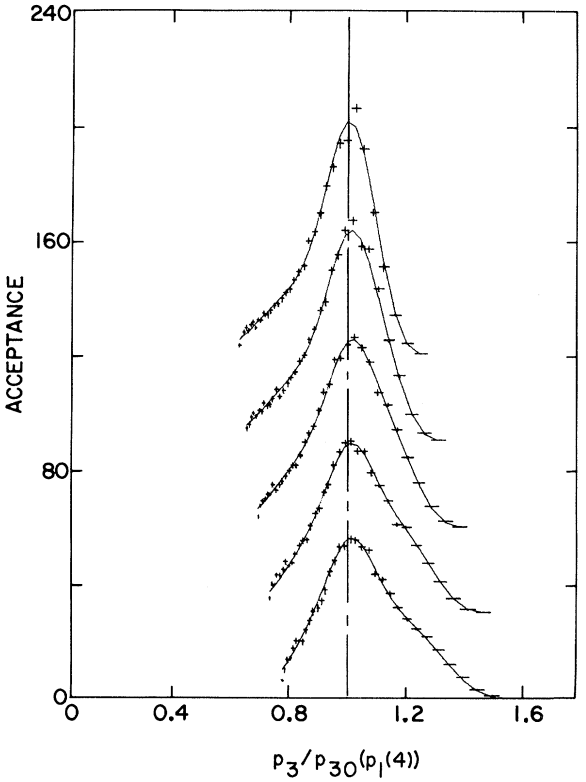

FIG. 8. The number of protons vs the ratio of the laboratory momentum of the recoil proton to the threshold recoil momentum when the incident momentum is that of the central bin. The five curves correspond to five approximately equally spaced beam momenta spanning the range of this experiment. For clarity each set has been displaced by 30 units relative to the next lower histogram with the highest momentum at the top. The smooth curves are fits to the data used to calculate the acceptance correction as explained in the text.

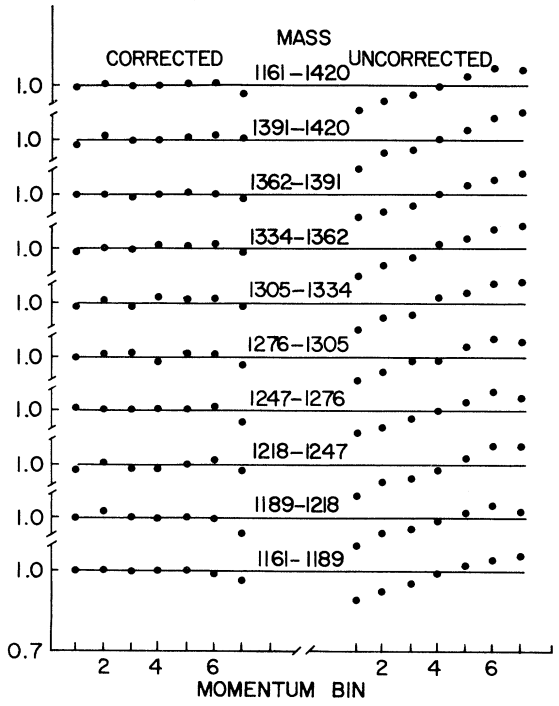

FIG. 9. The ratio of the cross section measured by a given momentum bin to the "average" cross section as explained in the text. The data are plotted for different mass bands as labeled with the sum over all masses at the top. The right-hand column shows the dependence of the cross section on momentum bin for the raw data. The left-hand column shows that this dependence vanishes after the acceptance correction is applied.

Since we measure seven different incident momenta at a single setting, these limits must be chosen to be slightly different for each of the seven different hodoscope elements. Since our detection efficiency at a given setting is a function of p_3, we must correct for this effect.

Figure 8 shows examples of the detection efficiency. The number of protons is histogrammed vs $p_3/p_{30}(p_1(4))$ where $p_{30}(p_1(4))$ is the momentum of a threshold proton coming from an interaction for which the beam momentum was that of the central momentum bin. Each data set is displaced, for clarity, by 30 units relative to the next lower histogram. The curves are fits to the histograms to furnish smooth parametrizations. The five distributions are from five approximately equally spaced beam momenta spanning the range covered by this experiment. The top curve is the highest momentum. As can be seen the acceptance function changes smoothly over the momentum range spanned.

For the jth momentum bin ($j=1-7$) the center of the band of protons we accept on one of these plots is shifted from that for the central ($j=4$) momentum bin by a factor $p_{30}(p_1(j))/p_{30}(p_1(4))$, where $p_1(j)$ is the incident momentum p_1 measured in the jth momentum bin. The ratio of the area under the curve in the band for the jth bin,

$$p_3 \pm \Delta p_3 = (1+S)p_{30}(p_1(j)) \pm f p_{30}(p_1(j)), \qquad (10)$$

to the area under the curve in the band for the fourth bin,

$$p_3 \pm \Delta p_3 = (1+S)p_{30}(p_1(4)) \pm f p_{30}(p_1(4)), \qquad (11)$$

gives the correction factor needed to normalize acceptances of each hodoscope bin.

The effects of this correction were verified by calculating the ratio of the cross section measured by each momentum bin to an "average" cross section at a given mass. The latter was calculated by fitting a smooth curve through several points centered on the point of interest. Figure 9 is a plot of this ratio vs momentum bin for all the data of set 3^- and for different mass ranges. The right-

hand column is uncorrected and shows that the cross section depends on the momentum bin. The left-hand column is corrected as explained above. After the correction the dependence disappears as desired.

C. Over-all consistency and stability

The cross section at each mass was measured several times at different incident-momentum settings by different momentum bins. These different independent measurements were used to verify the stability of the entire system and the consistency of the data within each data set. We define a normalized residual for the jth run at a mass m by

$$d_j = \frac{\sigma_j(m) - \langle\sigma(m)\rangle}{\Delta\sigma_j(m)}, \tag{12}$$

where $\sigma_j(m)$ is the cross section measured by the jth run and $\Delta\sigma_j(m)$ is its estimated error. $\langle\sigma(m)\rangle$ is the cross section averaged over all measurements at mass m. Since these are independent measurements, the distribution of the residuals should be a Gaussian with unit variance. Figure 10 shows the histogram of residuals for data set 3^-. The smooth curve is a best-fit Gaussian and has $\sigma = 1.1$. The deviation of σ from unity is a measure of our time-dependent systematic errors. Table II lists this quantity for each data set. All experimental error bars shown on the mass spectra have been scaled by the appropriate factor from Table II

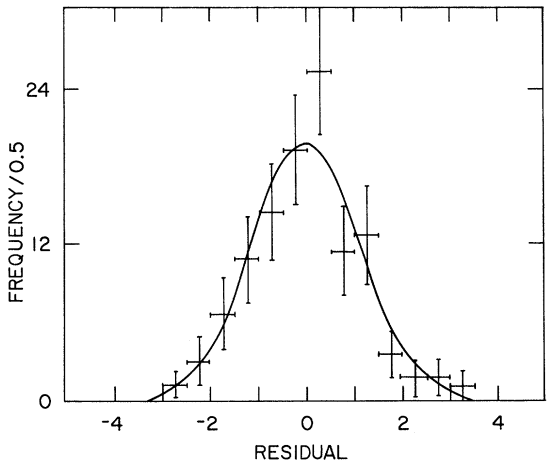

FIG. 10. Histogram of the normalized residuals of individual cross section measurements calculated by considering the deviations of the individual measurements from their average. To get the normalized residual this deviation is divided by the statistical error on the individual measurement, as explained in the text. The data are from data set 3^- and the smooth curve is a fitted Gaussian with $\sigma = 1.1$.

TABLE II. This table presents the standard deviations of Gaussian fits to the normalized residual distributions as described in the text. Results are presented for each data set. The errors on the mass spectra shown in Figs. 14, 16, 17, and 18 represent statistical errors that have been scaled by the appropriate entry in this table to account for systematic effects.

Data set	Standard deviation $S=-0.15$	$S=0$	$S=0.15$
1^+	1.18	1.34	1.51
2^+	1.00	1.09	1.31
3^+	1.11	1.17	1.32
1^-	1.17	1.51	1.65
2^-	1.12	1.14	1.26
3^-	1.06	1.10	1.39

and thus include these systematic errors.

To verify that there was no mass dependence in the distribution of these residuals we plotted residuals vs mass in Fig. 11 for data set 3^-. There is no significant correlation with mass in this or any of the other data sets.

IV. PRESENTATION AND ANALYSIS OF THE MEASURED MASS SPECTRA

Figure 12 shows a sample of π^- data taken with spectrometer settings tuned for 1.0, 0.9, and 0.8 times the momentum corresponding to threshold production. This corresponds to shifts in the spectrometer tune (as opposed to a shifted time-of-flight cut) of 0, −0.1, and −0.2, respectively. These data were taken in an attempt to observe A_2^- production at a smaller four-momentum transfer squared $-t$, while maintaining good resolution.

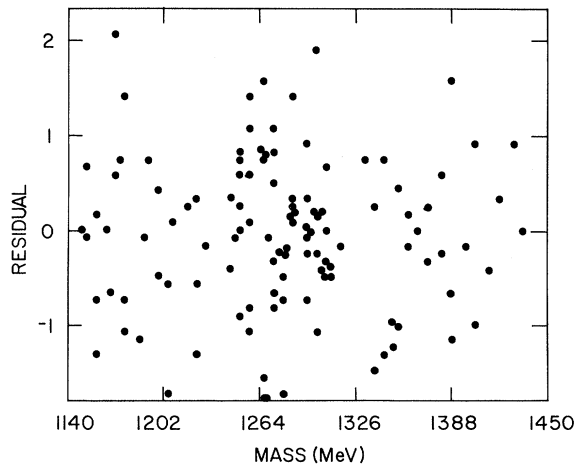

FIG. 11. Scatter plot of the normalized residuals of individual cross section measurements vs mass. The data are from data set 3^-.

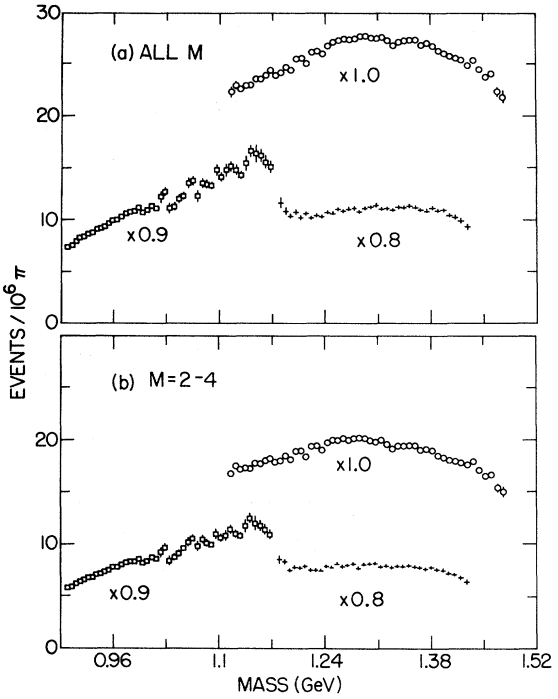

FIG. 12. A representative sample of negative spectra for different spectrometer settings presenting events/$10^6\pi$ versus mass. The data are for a shift +0.06 and a proton momentum bite of 0.22 (i.e., (+6±11)% bite): (a) for all final multiplicities and (b) for multiplicities $M=2$–4. The settings are for "tunes" of 1.0, 0.9, and 0.8 [see Eq. (8), text].

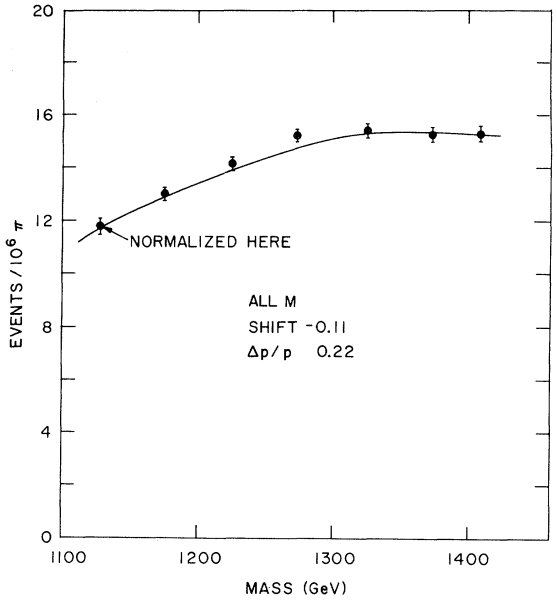

FIG. 13. A comparison of our data to a crude model of the background (shown as a solid curve). The background curve has been arbitrarily normalized to the data at one point. The data correspond to all multiplicities, a shift of 6% and a bite of 22%.

All charge multiplicities are shown in Fig. 12(a) and a subset of multiplicities are shown in Fig. 12(b). From a consideration of the known branching ratios for A_2 decay, multiplicities $M=3$–5 are expected to contain almost all of any real $A_2^{\pm}$ signal. All protons in the time-of-flight spectra (no $\Delta p/p$ cut) stored in the analyzer are shown.

The only general trend seen in the data as a function of "tune" is a change in yield as the tune is moved off the optimum threshold condition. No gain in possible A_2 signal-to-noise ratio was observed, and data taking with the spectrometer detuned was abandoned. The data at "times 0.9" were discussed in an earlier publication[6] and will not be considered here. The data at "times 0.8" will not be discussed further.

We had expected that the data would show a slowly changing background, possibly linear, as a function of mass, upon which even a small signal-to-noise ratio could be observed. Experimentally, a broad peaking of the background near the A_2 mass complicated the observation of an A_2 signal. Binnie's data[5] do not appear to exhibit this behavior and his spectrum falls slowly above 1180 MeV (see below). A crude estimate of the background shape was made to check our data. The sparse bubble-chamber cross-section data for various channels $\pi^- p \to p(n\pi)^-$ were assumed to follow phase space and subjected to the threshold kinematics of Sec. II above. Although the model is too crude to work well for individual multiplicities, it does show the general trend of Fig. 12 when averaged over all multiplicities.

Figure 13 shows the shape calculated from the model normalized to the data at a mass of 1132 MeV. The π^- data shown are for all multiplicities and for full width $\Delta p/p=0.22$ and shifted −0.11. The estimated background is normalized by 0.75 to match our measured data. The agreement is quite remarkable in view of the crudeness of the model and the data from which it was derived. At higher masses, the background spectra would probably fall smoothly since the total cross section has leveled out and many of the multipion thresholds have been passed. In addition, the $\pi^- p$ total cross section has a resonance at an equivalent mass of 1150 MeV and the $\pi^+ p$ total cross section has a resonance at 1350 MeV with each bump about 0.1 of the total cross section.

Figure 14 shows data from the data sets mentioned earlier for $\pi^{\pm}$ and for no shift with full width $\Delta p/p=15\%$. All multiplicities are shown in (a), (c), and (e) and $M=3$–5 are shown in (b), (d), and (f). The solid curves are the results of fits to a smooth background only. The background was

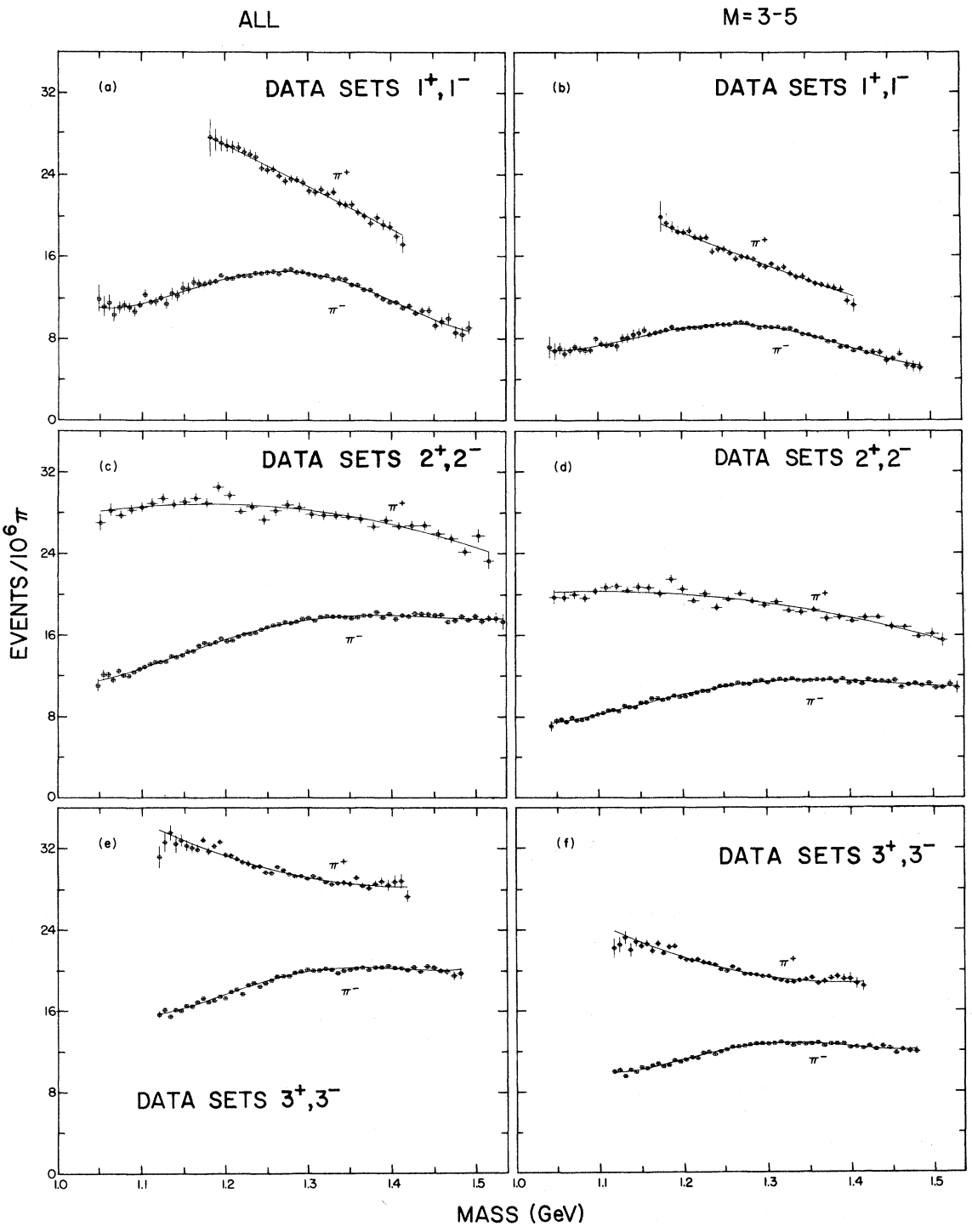

FIG. 14. Positive and negative spectra for data sets $1^{\pm}$, $2^{\pm}$, and $3^{\pm}$ for no shift with a momentum bite of ± 0.075. (a) all multiplicities and (b) $M = 3-5$ for data sets 1^{+} (π^{+}) and 1^{-} (π^{-}), respectively. (c) and (d) are the corresponding plots for data sets $2^{\pm}$ and (e) and (f) correspond to data sets $3^{\pm}$. The solid curves shown as fits to background only [see Eq. (13) in text].

TABLE III. Some parameters of fits to the data.

Data of Fig.	Parametrization	Probability	A_0(No./$10^6\pi$)	Mass (M)
14(a)π^+	Fourth order background only	0.995		
(a)π^-		0.999		
(c)π^+		0.000 02	...	
(c)π^-		0.767		
(e)π^+		0.041		
(e)π^-		0.0008		
(b)π^+	same	0.995		
(b)π^-		1.000		
(d)π^+		0.0002	...	
(d)π^-		0.848		
(f)π^+		0.247		
(f)π^-		0.025		
16(a) + 0.15	Plus "complex" B.W. M fixed	0.701	0 ± 0.02	1320 MeV
(a)0		1.000	0.24 ± 0.18	
(a) − 0.15		0.751	0.20 ± 0.08	
(c) + 0.15		0.0003	0.03 ± 0.11	
(c)0		0.900	0.16 ± 0.12	
(c) − 0.15		0.586	0.10 ± 0.07	
(e) + 0.15		0.036	0 ± 0.02	
(e)0		0.020	0 ± 0.09	
(e) − 0.15		0.735	0 ± 0.05	
(b) + 0.15	M free	0.963	0.83 ± 0.25	1194 ± 10
(b)0		1.000	0.25 ± 0.18	1331 ± 20
(b) − 0.15		0.722	0.21 ± 0.08	1323 ± 12
(d) + 0.15		0.136	0.73 ± 0.12	1282 ± 5
(d)0		0.928	0.26 ± 0.13	1292 ± 15
(d) − 0.15		0.671	0.17 ± 0.07	1293 ± 12
(f) + 0.15		0.162	0.40 ± 0.12	1251 ± 8
(f)0		0.134	0.47 ± 0.13	1287 ± 5
(f) − 0.15		0.745	0.09 ± 0.08	1283 ± 30
17(a)	M fixed	0.815	0 ± 0.16	1320 MeV
(c)		0.0002	0.37 ± 0.18	
(e)		0.0024	0 ± 0.13	
(b)	M free	0.788	0 ± 0.22	1273 ± 5
(d)		0.059	1.12 ± 0.19	1288 ± 5
(f)		0.040	0.74 ± 0.20	1267 ± 5

parametrized as a sum of Legendre polynomials in mass m' normalized to the interval (−1, 1):

$$\text{Events}/10^6\pi = B_0 + B_1 P_1(m') + B_2 P_2(m') + \cdots , \tag{13}$$

where $m' = (2m - m_{\min} - m_{\max})/(m_{\max} - m_{\min})$, the P_i are the Legendre polynomials of order i, and the B_i are adjustable coefficients. A χ^2 probability was used to test the goodness of fit and the sum was carried to the lowest order yielding a satisfactory fit (approximately better than 1%). All twelve fits are acceptable at fourth order with the fit parameters listed in Table III. The solid curves go smoothly through the data and give no indication of an $A_2^{\pm}$ signal.

In order to quantify the presence or absence of $A_2^{\pm}$, we made additional fits to the background form in (13) plus a Breit-Wigner resonance. Two parametrizations of the Breit-Wigner (BW) form were used: a "simple" nonrelativistic one

$$\text{Simple BW} = A_0 \frac{(\frac{1}{2}\Gamma_0)^2}{(E - E_0)^2 + (\frac{1}{2}\Gamma_0)^2} \tag{14}$$

and a "complex" relativistic one

$$\text{Complex BW} = A_0 \frac{E_0 E \Gamma(E_0)\Gamma(E)}{(E_0^2 - E^2)^2 + E^2\Gamma^2} , \tag{15}$$

where A_0 is an adjustable parameter (the number of resonant events/$10^6\pi$), E is the mass, E_0 the resonance mass, and Γ_0 the resonance width. The energy-dependent width $\Gamma(E)$ in the complex rela-

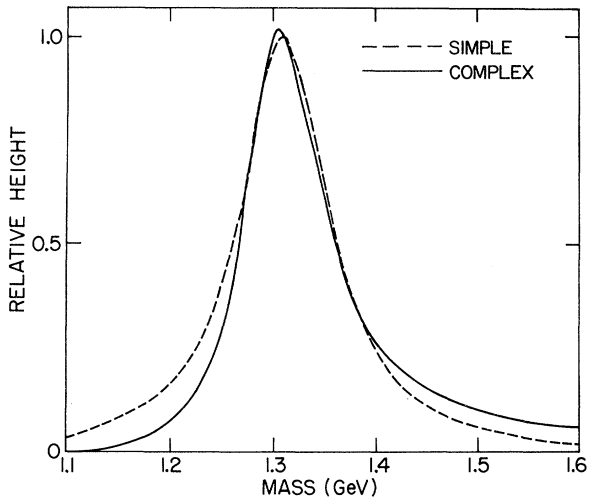

FIG. 15. Comparison of the "simple" and "complex" Breit-Wigner forms used in fitting the data. In this plot the mass and width parameters are fixed at $E_0 = 1310$ MeV and $\Gamma_0 = 100$ MeV, the current Particle Data Group values for the A_2 mass and width.

tivistic form (15) is

$$\Gamma(E) = r_1\Gamma_1 + r_2\Gamma_2 + r_3\Gamma_3 , \tag{16}$$

where r_i and Γ_i are the branching ratio and partial width for the three decay modes $\rho\pi$, $\eta\pi$, and $K\bar{K}$ ($r_1 = 0.724$, $r_2 = 0.153$, $r_3 = 0.047$) with

$$\Gamma_i = \Gamma_0 (q_i/q_{i0})^{2l_i+1} \rho(q_i)/\rho(q_{i0}) \tag{17}$$

and

$$\rho(q) = (q + 3R^2q^2 + R^4q^4)^{-1} . \tag{18}$$

The q_i are the decay rest-frame momenta from mass E in mode i, q_{i0} are the values of q_i for the resonance mass E_0, $R^2 = 12$ GeV^{-2}, and $l_1 = l_2 = l_3 = 2$. Figure 15 shows a comparison of the "simple" (dotted) and "complex" (solid) forms with $A_0 = 1$, $E_0 = 1310$ MeV, and $\Gamma_0 = 100$ MeV. These values for E_0 and Γ_0 correspond to the current Particle Data Group values[10] for the A_2 mass and width.

Figure 16 shows the $M = 3$–5 π^- data of Fig. 14 together with additional data for shifts of ± 0.15 with fits to background plus resonance. In each case the bite widths are 0.15 (± 0.075), so that the data points are disjoint samples. Figures 16(a), 16(c), and 16(e) use the "complex" form (15) with the amount of A_2 allowed to vary but with the mass and width of the Breit-Wigner constrained to the current Particle Data Group values ($E_0 = 1320$ MeV, $\Gamma_0 = 100$ MeV). Figures 16(b), 16(d), and 16(f) also use the "complex" form but with only the width fixed at $\Gamma_0 = 100$ MeV and both the amount and mass (A_0 and E_0) free to be fitted. No consistency in the amount of A_2 required or of the mass (when not constrained) as determined by the fits was found between the different data sets. Similar results (not shown) were found when the fits were repeated with the "simple" form (14) or when the width was also allowed to be fitted. Some of the fitted parameters are given in Table III. Moreover, as the order n of the background was increased, the amount of A_2 (i.e., the A_0 coefficient) required tended to zero, and good fits with $A_2^{\pm}$ are not obtained with a lower-order n than the background only fits.

In order to improve the statistical accuracy, the sum of the data in the six subsets of Fig. 16 [(a), (b), (c), (d), (e), and (f)] were similarly fitted. The results of these fits are given in Table III and Fig. 17. Again no consistency is found for the amount of A_2^- or its parameters.

The first data set 1^- showed some possible "splitting" which was not supported by additional data (sets 2^- and 3^-). However, fits to a dipole resonance [convoluted with a Gaussian resolution function of $\Gamma = 12$ MeV (FWHM)] plus background were performed. The "dipole" resonance is parametrized as

$$\text{Dipole BW} = A_0 \frac{(E_0 - E)^2\Gamma_0^2}{(E_0 - E)^2 + \frac{1}{4}\Gamma_0^2} , \tag{19}$$

with $\Gamma_0 = 28$ MeV. The $M = 3$–5 $\pi^{\pm}$ data of Figs. 14(b), 14(d), and 14(c) are shown with the dipole-plus-background fits in Fig. 18. A negligible amount of dipole $A_2^{\pm}$ was needed.

Since the A_2 signals are expected to be almost entirely in the $M = 3$–5 sample, the ratio

$$R = \frac{(\text{Number of events with } M = 3\text{–}5)}{(\text{All events}) - (\text{Number with } M = 3\text{–}5)} \tag{20}$$

can also be plotted in order to detect a small A_2 signal while minimizing the effect of the broad bump in the background.[11] The smooth curves in Fig. 14 provide a very good representation of the data without the statistical wiggles. The ratio R was calculated for the data in Fig. 14 using the parameters of the fitted curves. The ratios R for the six data sets are shown in Fig. 19. The ratios vary smoothly with no indication of an A_2 signal. We also indicate in this figure what we would expect for an A_2 production cross section of $(E^*/p^*)(\Delta\sigma/\Delta m) = 180$ μb/12 MeV (see Sec. V below for a discussion of this value). Note that although data set 3^- has a "peak" of about the same magnitude as the "expected" curve, it is twice the known width of the A_2.

In summary, we conclude from the above discussion that our data do not require any $A_2^{\pm}$ production at threshold. Upper limits can be inferred from Table III and are given in the discussion below.

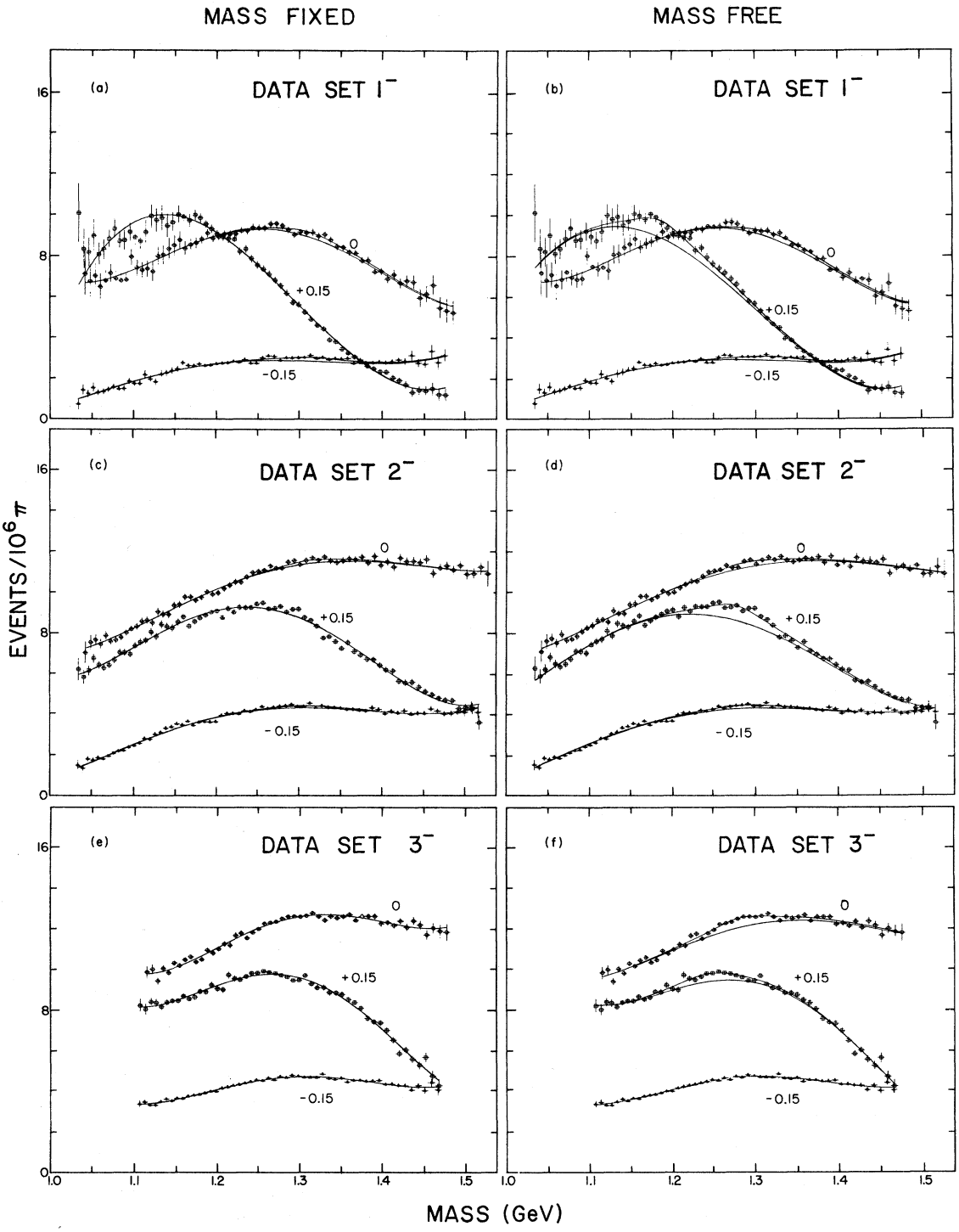

FIG. 16. Fits of background plus a Breit-Wigner curve (A_2 signal) to negative spectra with multiplicities $M = 3$–5 for three different cuts on the recoil proton momentum. The cuts correspond to shifts of +0.15, 0, and −0.15 and the bite widths are 0.15 (± 0.075) so that the cuts correspond to disjoint samples of data. (a), (c), and (e) are fits using a "complex" Breit-Wigner form [Eq. (14)] with the mass and width parameters constrained to the current Particle Data Group values of $E_0 = 1320$ MeV and $\Gamma_0 = 100$ MeV but with the amount of A_2 (Breit-Wigner amplitude A_0) free to be fit. In (b), (d), and (f) [same data as in (a), (c), and (e), respectively] the fits were repeated but with only the width parameter constrained to $\Gamma_0 = 100$ MeV. (a) and (b) are from data set 1^-, (c) and (d) are from data set 2^-, and (e) and (f) are from data set 3^-. The data with a shift of 0 are the same data shown in Fig. 14.

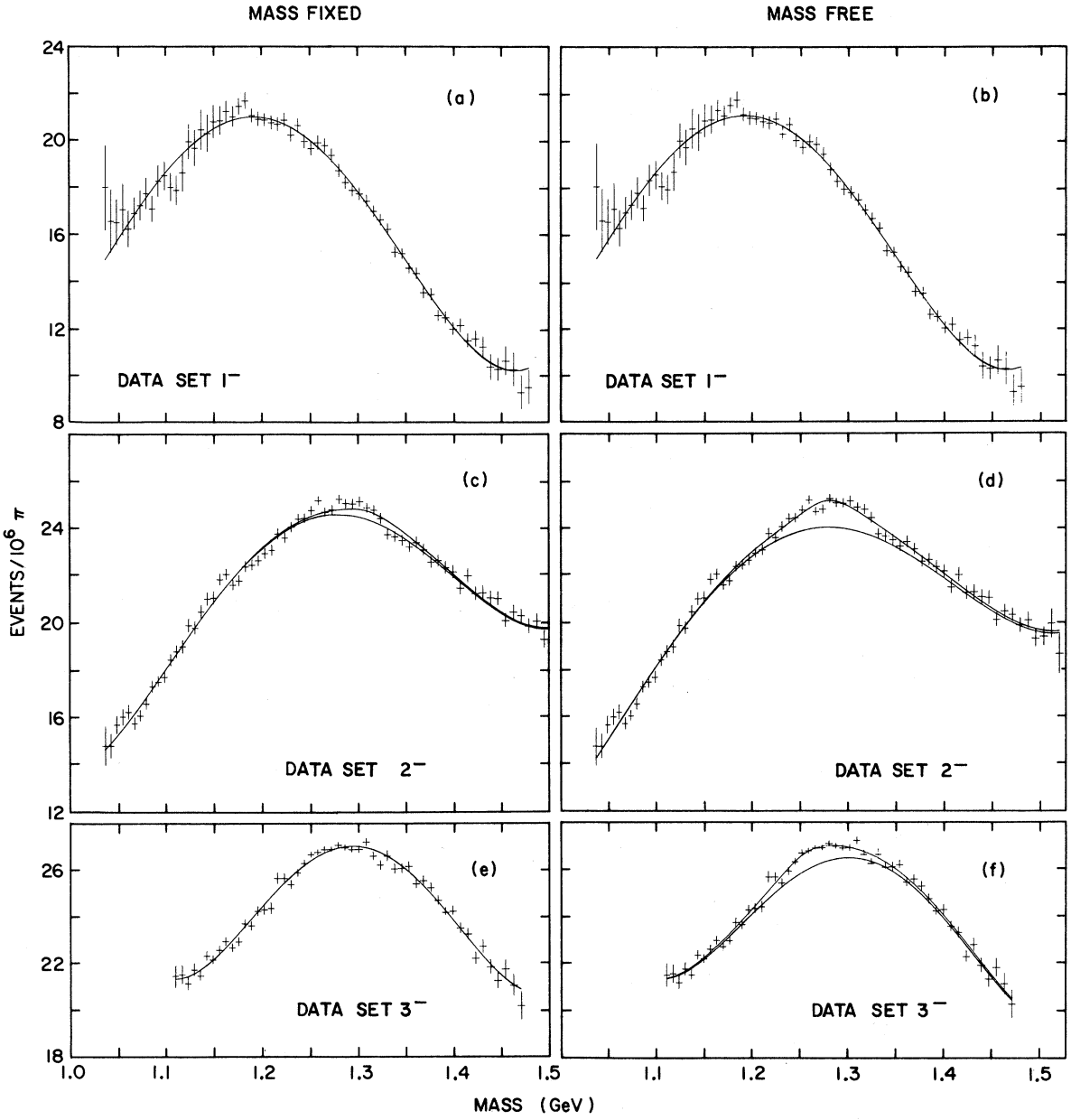

FIG. 17. The data of Fig. 16 summed over all shifts and resulting in an average shift of 0 with a bite of 0.45 [i.e., $(0 \pm 22.5)\%$]. Fits with the mass and width constrained are on the left [(a), (c), and (e)] and fits with only the width constrained are in the right [(b), (d), and (e)]. In each case data sets 1^-, 2^-, and 3^- go from top to bottom.

V. DISCUSSION

The upper limit on A_2 production at threshold from this experiment is $(E^*/p^*)(\Delta\sigma/\Delta m) < 40$ μb/12 MeV (95% confidence level). This appears to be inconsistent with the result of Binnie *et al.*[5] In Fig. 20 we show his data, taken from Fig. 2 of Ref. 5, together with fits which we have made to that data. The solid curve in Fig. 20(a) is the result of our fit if we assume the presence of both background and an A_2 signal. The results of this fit agree with those of Binnie *et al.* In Fig. 20(b) we show the results of a fit to these data which assumed the presence of a smooth background only. Although the confidence level of this fit is poor ($\sim 10^{-3}$), the fit is not totally rejected. Thus, at the three-standard-deviation level we can fit the data of Binnie *et al.* with no A_2. If we choose a more conservative level of two standard devia-

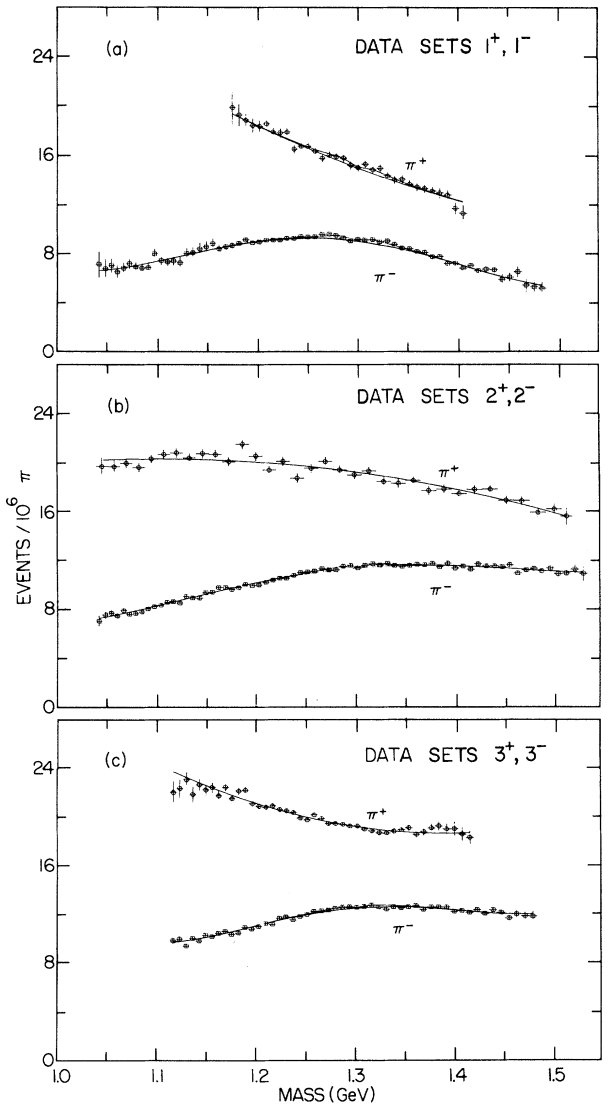

FIG. 18. The $\pi^{\pm}$ data of Figs. 14(b), 14(d), and 14(f) [$M = 3-5$, $(0 \pm 7.5)\%$] refitted to background plus a "dipole" resonance [Eq. (19), see text].

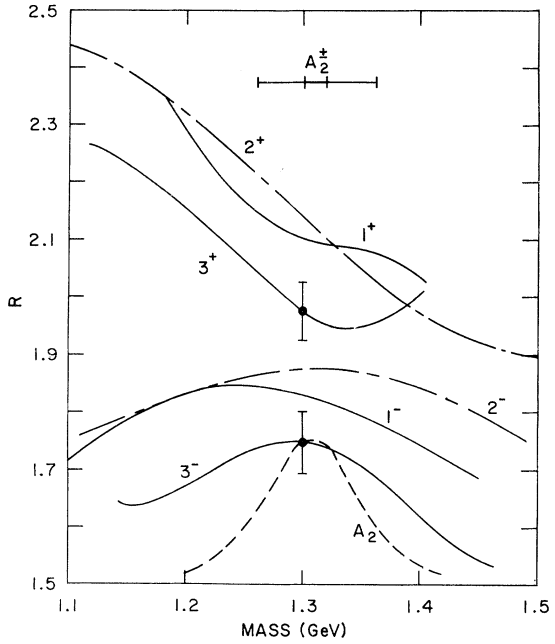

FIG. 19. Ratio $R = \sigma(3-5)/\sigma(<3, >5)$ of data with $M = 3-5$ to data with $M \neq (3-5)$ versus mass for data sets $1^{\pm}$, $2^{\pm}$, and $3^{\pm}$. The fits to background only shown in Fig. 14 were used as a parametrization of the data for the determination of this ratio. Any $A_2^{\pm}$ signals are expected to contribute to the numerator only and appear as a bump of the order of magnitude of one third or more of the dashed A_2 curve shown. No definite A_2 signals are observed. The vertical error bars represent the approximate point to point errors in the data. The horizontal bar is centered on the A_2 mass and indicates the mass uncertainty and the width of the A_2.

tions to estimate a lower limit of A_2 required by their data, then our interpretation if 50 μb/12 MeV $< (E^*/p^*)(\Delta\sigma/\Delta m) < 100$ μb/12 MeV for A_2^- production at threshold. Although some of our data sets could accommodate A_2 production at this level, a consideration of all of our data yields an upper limit of 40 μb/12 MeV.

In Table IV we present the values of A_2^- cross sections measured in other experiments.[12-18] The last column of the table gives the value of $(E^*/p^*)(\Delta\sigma/\Delta m)$ in units of μb/12 MeV. If the A_2 cross section were all due to s-wave production then this quantity should be constant, independent of p^*/E^*. Although the results of these experiments are all consistent with their average value of 180 ± 15 μb/12 MeV, A_2 production above threshold is found to be strongly peaked forward so that waves higher than s wave must also be present. For $p^* \lesssim 100$–140 MeV/c (i.e., for $p^*/E^* \lesssim 0.04$) s wave must dominate and thus our data and the data of Binnie *et al.* limit the amount of s-wave A_2 production. In Fig. 21 we present the values of $(E^*/p^*)(\Delta\sigma/\Delta m)$ for our data, the data of Binnie *et al.*, and the experiments listed in Table IV. The average value of the data in Table IV is shown in the horizontal hatched region and is inconsistent with our data and the data of Binnie *et al.* Thus the rapid rise in the A_2 cross section is not due to s-wave production. (This is in contrast to η production in $\pi^- p \to n\eta$, for instance, where the cross

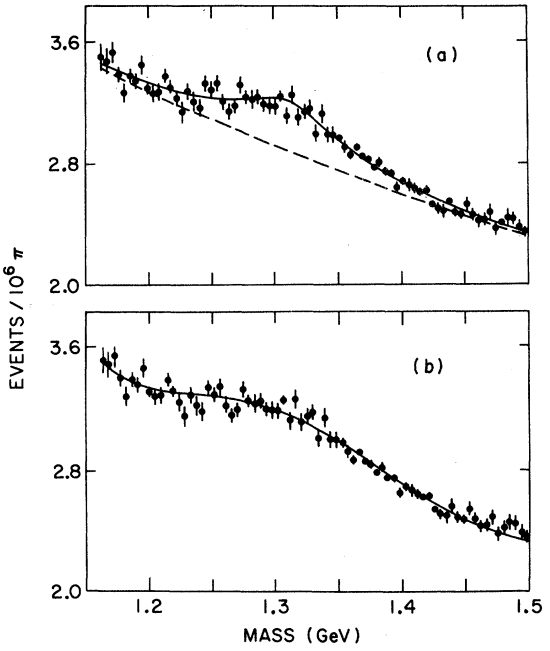

FIG. 20. Our fits to the $(3\pi)^-$ data of Binnie *et al.* (Fig. 2 of Ref. 3): (a) background plus A_2 resonance as fitted by Binnie and (b) background only. Our fit (a) agrees with Binnie's fit. Fit (b) has a worse χ^2 but is not totally rejected.

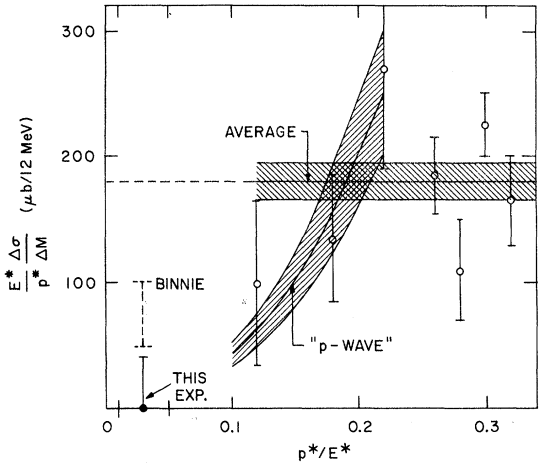

FIG. 21. The invariant A_2^- cross section (E^*/p^*) $\Delta\sigma/\Delta M$ versus p^*/E^*. The data of Table IV (Refs. 12 to 18) are shown as open circles. The range of the amount of A_2 which Binnie's data (Fig. 2 of Ref. 3) can accomodate according to our fits is shown as a dashed line (see text). This experiment is plotted as a solid point with error bars. The p-wave curve appears to agree with the results of this experiment and of Binnie *et al.* near threshold.

section $\Delta\sigma/\Delta m$ falls after it reaches a maximum at a p^* of 100 MeV/c due almost entirely to the s-wave component.) A cross section due to p-wave production would rise as p^{*2} and this behavior is indicated as the curved hatched region in Fig. 21. All data below p^*/E^* of 0.2 are consistent with this behavior.

A possible explanation of the lack of A_2 s-wave production would be if the rapid rise above threshold were due to direct channel resonances. The nucleon and Δ resonances in the region of center-of-mass energy corresponding to A_2 production at threshold (2200–2400 MeV) all have high angular momentum and can only feed p-wave or higher proton-A_2 final states.

TABLE IV. $A_2^-(1310, 100)$ cross sections.

Ref.	P_{lab} (GeV/c)	σ_{A_2} (μb)	Mass (M) (MeV)	ΔM (MeV)	$\frac{P^*}{E^*}$	$\frac{E^*}{P^*}\frac{\Delta\sigma}{\Delta M}$ (μb/12 MeV)
•••	2.2 (Threshold)	•••	•••	•••	0	•••
12	2.26	135 ± 60	1260 [a]	40 [a]	0.12	<500 [a]
13	2.36	85 ± 55	1310	80–90 [b]	0.12	100 ± 65
13	2.60	205 ± 70	1310	100	0.18	135 ± 50
13	2.86	490 ± 140	1310	100	0.22	270 ± 80
13–15	3.1–3.22	400 ± 60 [c]	1310	100	0.26	185 ± 30
16	3.65	250 ± 85	1310	100	0.28	110 ± 40
17, 18	3.9	560 ± 60 [c]	1310	100	0.30	225 ± 25
14, 15	4–4.2	435 ± 85 [c]	1310	100	0.32	165 ± 35
					Average	180 ± 15

[a] Too close to threshold to observe the full width of the A_2. Used as an upper limit (~16 events, poor statistics).

[b] This is an estimate of the observed range of A_2 masses at this distance above threshold.

[c] Average of values given in references.

ACKNOWLEDGMENTS

We wish to express our thanks to the entire AGS staff for their support during this experiment. In addition, we thank Professor F. Sannes for his help in the early stages of the experiment and with a large part of the electronics setup. We acknowledge the help of C. Rago and J. Cickay with the data taking and analysis. We also thank Dr. T. Kycia, Dr. S. Ozaki, and Dr. F. Turkot for the helpful loan of some equipment. Finally thanks are due Professor B. Maglich and Dr. N. P. Samios for their support and encouragement.

---

*Work performed under the auspices of the Energy Research and Development Administration, and in part by the National Science Foundation.

†Present address: Boeing Computer Services, Scott Plaza, 2 Industrial Highway, Philadelphia, Pennsylvania 19113.

‡Present address: Physics Department, Brookhaven National Laboratory, Upton, New York 11973.

§Present address: Department Saturne, CEN/Saclay, 91190 Gif-sur-Yvette, France.

‖Research supported in part by the National Science Foundation.

¶Present address: American Electric Power Service Company, 2 Broadway, New York, New York.

**Present address: Fermi National Accelerator Laboratory, P. O. Box 500, Batavia, Illinois 60510.

††Work supported in part formerly by the U. S. Atomic Energy Commission under Contract No. AT(11-1)-2009, Task A, and the Indiana University Foundation.

[1]G. Chikovani *et al.*, Phys. Lett. 25B, 44 (1967).

[2]See, for instance, C. M. Ankenbrandt *et al.*, Phys. Rev. Lett. 29, 1688 (1972) or Particle Data Group, Phys. Lett. 39B, 1 (1972) for many references to the A_2 controversy. A more recent result not included there is D. Underwood *et al.*, Phys. Rev. D 11, 2345 (1975).

[3]See B. Maglich, in *Proceedings of the Fifth International Conference on Elementary Particles, Lund, 1969,* edited by G. von Dardel (Berlingska Boktryckeriet, Lund, Sweden, 1970), p. 293 for a summary of models proposed for A_2 splitting.

[4]See Ref. 6 below for a discussion of the situation in this mass region and for references to other experiments.

[5]D. M. Binnie *et al.*, Phys. Lett. 36B, 257 (1971).

[6]G. R. Kalbfleisch *et al.*, Nucl. Phys. B69, 279 (1974).

[7]W. C. Harrison *et al.*, Bull. Am. Phys. Soc. 18, 125 (1973), paper JK7.

[8]B. Maglich and G. Costa, Phys. Lett. 18, 185 (1965).

[9]G. Conforto *et al.*, Phys. Lett. 45B, 154 (1973); G. Grayer *et al.*, *ibid.* 34B, 333 (1971).

[10]Particle Data Group, Phys. Lett. 50B, 1 (1974).

[11]We thank Dr. K. W. Lai for suggesting that a ratio test be made on the data.

[12]R. P. Weickowicz *et al.*, Phys. Lett. 28B, 199 (1968).

[13]L. D. Jacobs, UCRL Report No. UCRL-16877, 1966 [Ph.D. thesis (unpublished)], p. 156.

[14]O. I. Dahl *et al.*, Phys. Rev. 163, 1377 (1967).

[15]S. U. Chung *et al.*, Phys. Rev. 165, 1491 (1968); Phys. Rev. Lett. 18, 100 (1967).

[16]G. Benson *et al.*, Phys. Rev. Lett. 16, 1177 (1966).

[17]P. G. Wohlmut *et al.*, Nucl. Phys. B18, 505 (1970).

[18]M. J. Losty *et al.*, Phys. Lett. 56B, 96 (1975).